JACS
JOURNAL OF THE AMERICAN CHEMICAL SOCIETY
Article
pubs.acs.org/JACS

Constructing Three-Dimensional Mesoporous Bouquet-Posy-like TiO_2 Superstructures with Radially Oriented Mesochannels and Single-Crystal Walls

Yong Liu,[†,‡,#] Kun Lan,[†,#] Shushuang Li,[†] Yongmei Liu,[†] Biao Kong,[†] Geng Wang,[§] Pengfei Zhang,[†] Ruicong Wang,[†] Haili He,[†] Yun Ling,[†] Abdullah M. Al-Enizi,[∥] Ahmed A. Elzatahry,[⊥] Yong Cao,[†] Gang Chen,[§] and Dongyuan Zhao*[,†]

[†]Department of Chemistry, Shanghai Key Laboratory of Molecular Catalysis and Innovative Materials, Laboratory of Advanced Materials, iChEM (Collaborative Innovation Center of Chemistry for Energy Materials), Fudan University, Shanghai 200433, China
[‡]Department of Chemistry, University of California, Berkeley, California 94720, United States
[§]School of Physical Science and Technology, ShanghaiTech University, Shanghai 201210, China
[∥]Department of Chemistry, College of Science, King Saud University, Riyadh 11451, Saudi Arabia
[⊥]Materials Science and Technology Program, College of Arts and Sciences, Qatar University, P.O. Box 2713, Doha, Qatar

Supporting Information

ABSTRACT: Constructing three-dimensional (3-D) hierarchical mesostructures with unique morphology, pore orientation, single-crystal nature, and functionality remains a great challenge in materials science. Here, we report a confined microemulsion self-assembly approach to synthesize an unprecedented type of 3-D highly ordered mesoporous TiO_2 superstructure (Level-1), which consists of 1 spherical core and 12 symmetric satellite hemispheres epitaxially growing out of the core vertices. A more complex and asymmetric TiO_2 superstructure (Level-2) with 13 spherical cores and up to 44 symmetric satellite hemispheres can also be well manipulated by increasing the size or content of impregnated TiO_2 precursor emulsion droplets. The obtained 3-D mesoporous TiO_2 superstructures have well-defined bouquet-posy-like topologies, oriented hexagonal mesochannels, high accessible surface area (134−148 m^2/g), large pore volume (0.48−0.51 cm^3/g), and well single-crystalline anatase walls with dominant (001) active facets. More interestingly, all cylindrical mesopore channels are highly interconnected and radially distributed within the whole superstructures, and all TiO_2 nanocrystal building blocks are oriented grown into a single-crystal anatase wall, making them ideal candidates for various applications ranging from catalysis to optoelectronics. As expected, the bouquet-posy-like mesoporous TiO_2 superstructure supported catalysts show excellent catalytic activity (≥99.7%) and selectivity (≥96%) in *cis*-semihydrogenation of various alkynes, exceeding that of commercial TiO_2 (P25) supported catalyst by a factor of 10. No decay in the activity was observed for 25 cycles, revealing a high stability of the mesoporous TiO_2 superstructure supported catalyst.

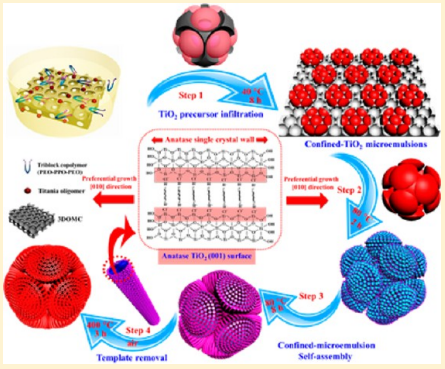

1. INTRODUCTION

A challenging goal in materials chemistry and physics is spontaneously to design intended inorganic mesoporous superstructures with unprecedented architectural complexity and symmetry.[1−16] Owing to the organized mesostructures, such superstructures are theoretically and practically proven to have remarkably tunable catalytic, electronic, magnetic, and optical properties, which promise various applications ranging from catalysis to optoelectronics.[17−25] Despite recent biological success in biomaterials-based hierarchical-assembly,[26−29] few mesostructures with high levels of architectural symmetry have been demonstrated. The major synthetic obstacle to such ordered mesoporous superstructures mainly arises from the lack understanding of growth mechanisms enabling unprecedented levels of mesostructure control in different compartments of the same particle.[30] In this regard, identifying such anisotropic growth mechanisms of mesostructures would enable access to ordered functional superstructure with a high degree of architectural complexity yet highly controlled symmetry and morphology.[31]

Additionally, nanoscale alignment of the mesopore channels and control of the periodic crystalline atomic lattice within the mesostructure are also greatly challenging but highly desirable for applications.[32−37] For example, if the well-defined mesopores and atomic lattices are assembled into one crystal in a periodic array, the electrical, catalytic, and optical properties of the mesoporous inorganic solids are confirmed

Received: November 9, 2016
Published: December 12, 2016

DOI: 10.1021/jacs.6b11641
J. Am. Chem. Soc. 2017, 139, 517−526

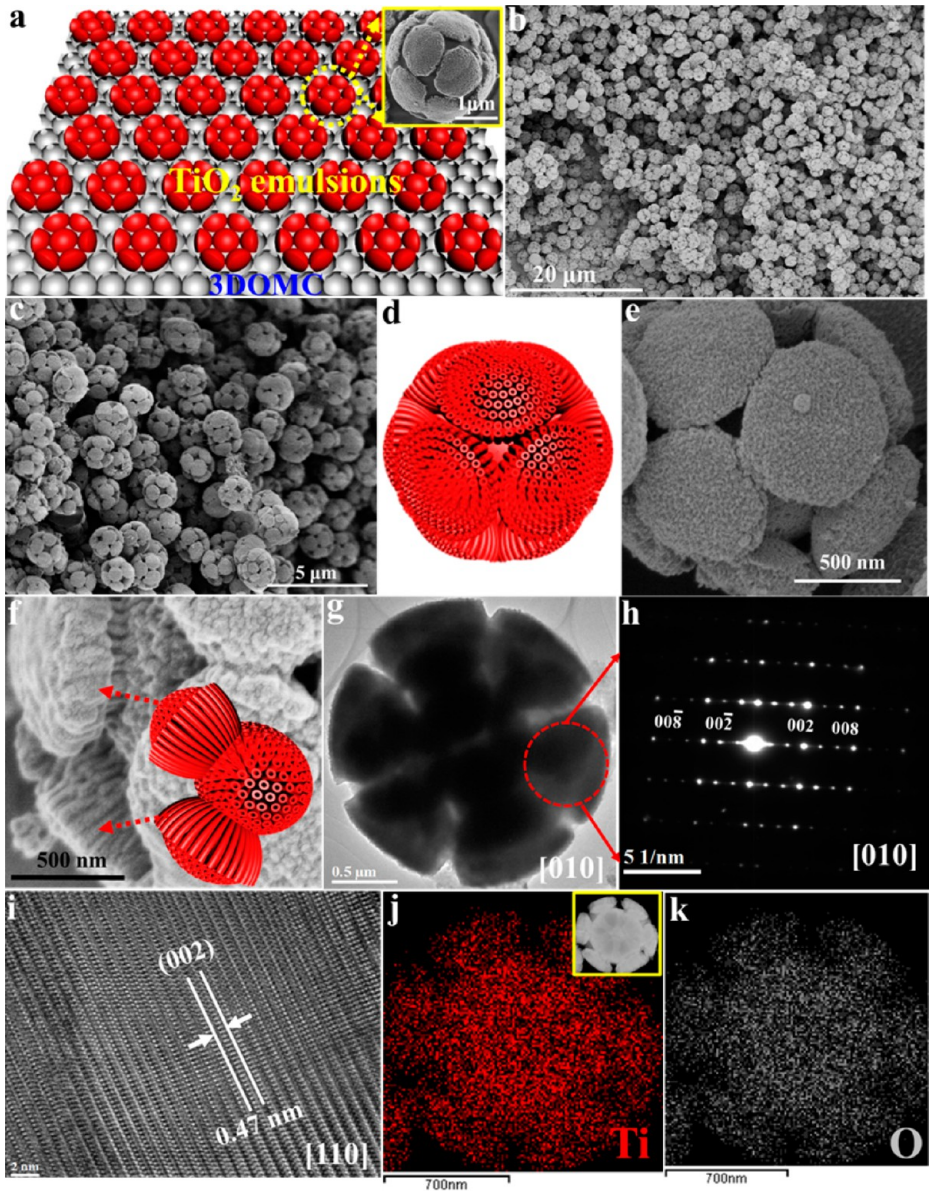

Figure 1. Three-dimensional (3-D) mesoporous bouquet-posy-like TiO_2 superstructures (Level-1). (a) Schematic representation of nucleation and growth of the Level-1 3-D bouquet-posy-like TiO_2 gel microemulsions (~2 μm in diameter) within 3-D ordered macroporous carbon (3DOMC) scaffolds. Inset of panel a is the Cryo-SEM image of a single as-made Level-1 TiO_2 gel microemulsion taken out from the cracked 3DOMC. Before the electron microscopy analysis, the TiO_2 gel microemulsion was frozen by soil nitrogen. (b, c) SEM images of the Level-1 mesoporous TiO_2 superstructure after calcination in air at 400 °C for 2 h. (d) The structure model of a Level-1 mesoporous TiO_2 superstructure, showing its 3-D bouquet-posy-like topology (1 spherical core and 12 satellite hemispheres with 6-fold symmetry) with radially oriented mesopore channels. (e, f) High-magnification SEM image of a single Level-1 mesoporous TiO_2 superstructure. Inset of panel f is the structure model of the interior radially oriented mesopore channels within a Level-1 mesoporous TiO_2 superstructure, showing that cylindrical mesochannels are highly interconnected between spherical core and satellite hemispheres. (g) TEM image of a single Level-1 mesoporous TiO_2 superstructure recorded along [110] and [010] zone axis. (h) The SAED pattern taken from the dotted square area marked in panel g. (i) HRTEM image taken from the area of the cylindrical mesopore bundles of an ultramicrotomed Level-1 mesoporous TiO_2 superstructure with [110] incidence. (j, k) EDX elemental maps of Ti and O recorded on a single Level-1 mesoporous TiO_2 superstructure. Inset of panel j is the corresponding high-angle annular dark-fields scanning TEM (HAADF-STEM) image.

to be greatly modified. Up to now, only a few groups have reported alignment control of tubular mesopores in mesoporous silica using air flow,[38] electric fields,[39] and magnetic field.[40] Recently, we have reported full orientation control of both mesopore channels and nanocrystal building blocks within mesoporous TiO_2 microspheres using an evaporation-driven oriented assembly method.[41,42] Despite all of above efforts, to date, full alignment control of mesopore channels and crystalline atomic lattice within a hierarchical mesoporous superstructure crystal has not yet been achieved and remains a big challenge in materials science.

2. RESULTS AND DISCUSSION

Here we demonstrate a confined microemulsion self-assembly approach that is capable of organizing 3-D highly ordered mesoporous TiO_2 superstructures with unprecedented bouquet-posy-like topologies, radially oriented mesochannels, and single-crystal walls. By controlling the size or content of TiO_2

DOI: 10.1021/jacs.6b11641
J. Am. Chem. Soc. 2017, 139, 517−526

precursor emulsion droplets, the levels of architectural complexity and symmetry can be well manipulated. Typically, a mesoporous bouquet-posy-like TiO_2 superstructure (Level-1) consisting of 1 spherical core and 12 symmetric satellite hemispheres is obtained by confined growth of the TiO_2 emulsion droplets within a 3-D ordered macroporous carbon (3DOMC) scaffold. The 3DOMC scaffolds with uniform cavities of ~800 nm and connecting windows of ~200 nm here were prepared as confined space (Figure S1).[43] A key feature of the 3DOMC scaffolds is that their highly ordered domains are ultralarge, over >1 cm^2, with face-centered cubic (*fcc*) structure. Such long-range regularity and perfection are essential, as it permits the formation of uniform inverse colloid architectures.

The confined microemulsion self-assembly process within 3DOMC scaffolds starts with the solid−liquid interface separation caused by the preferential evaporation of tetrahydrofuran (THF) solvent at a low temperature of 40 °C for 20 h, resulting in a multicompartment TiO_2 gel microemulsion droplet within 3DOMCs with a size of ~2.0 μm (Figure 1a and Figure S2). The as-made flexible TiO_2 gel microemulsion droplets are constructed of one spherical core and 12 symmetric hemispheres growing out from the neighboring connected windows of macroporous cavities of 3DOMCs (Figure S2a−c). Continuous evaporation of the residual THF and hydrolyzed solvents within TiO_2 gel microemulsion subsequently at 80 °C drives the oriented growth of both mesopore channels and periodic anatase atomic lattice along the free radial direction.[42] This yields 3-D open mesoporous bouquet-posy-like TiO_2 superstructures with radially oriented mesopore channels and single-crystalline anatase walls. Low-magnification scanning electron microscopy (SEM) images show that the products consist of a large quantity of uniform 3-D mesoporous bouquet-posy-like TiO_2 superstructures (Level-1) with an average diameter of ~1.6 μm after removal of 3DOMC scaffolds by calcination in air at 400 °C for 2 h (Figure 1b and Figure S3a,b). Close inspection of the Level-1 TiO_2 superstructures by high-magnification SEM images (Figure 1c and Figure S3b−d) reveals that they possess 1 spherical core and 12 satellite hemispheres with a 6-fold symmetry. The high-magnification SEM images in Figure 1e, Figure S3d and Figure S4 clearly show that open mesopores are well exposed on the rough hemisphere surface and extended throughout the whole Level-1 TiO_2 superstructure. More interestingly, all cylindrical mesopore channels are well interconnected between spherical core and 12 satellite hemispheres (Figure 1f). The pore size is roughly estimated to be about ~6.0 nm from the high-magnification SEM images (Figure 1e and Figure S3c,d). Transmission electron microscopy (TEM) images of a single Level-1 mesoporous TiO_2 superstructure (Figure 1g and Figure S3e−h) recorded along [110] and [010] zone axes show well-defined 6-fold symmetry, where one spherical core (~800 nm in diameter) is combined with six couples of hemispherical posies (~400 nm in diameter) in the plane. To confirm the interior structure, the Level-1 mesoporous TiO_2 superstructures were ultramicrotomed. The section TEM images of a single Level-1 TiO_2 superstructure show that the ordered cylindrical mesopore channels are highly interconnected and distributed radially from the center to the surface within both spherical core and hemispherical posies (Figure S5a,b and Figure S6).

High-resolution TEM (HRTEM) images and selected-area electron diffraction (SAED) patterns further confirm that each individual mesoporous hemispherical posy unit (about 0.4 × 0.7 μm^2 in domain size) has single-crystal anatase nature (Figure 1h,I and Figure S5c,d). The HRTEM image recorded on a single ultramicrotomed wall with [001] incidence shows the (200) and (020) atomic planes of anatase with a lattice spacing of 0.19 nm and an interfacial angle of 90° (Figure S5c), suggesting that the (001) atomic plane is the dominantly exposed facet along the mesopore walls.[44,45] The SAED pattern in Figure 1h can be well indexed into diffraction spots of the single-crystal anatase along [010] zone. High-angle annular dark-fields scanning TEM (HAADF-STEM) images of a single Level-1 mesoporous TiO_2 superstructure clearly confirm the hierarchical bouquet-posy-like morphology with a spherical core and six couples of hemispherical posies (inset of Figure 1j). The elemental mapping taken from the HAADF-STEM image shows that only Ti and O elements are uniformly distributed on the whole superstructure (Figure 1j,k), confirming a pure anatase nature of the Level-1 mesoporous TiO_2 superstructures.

Wide-angle X-ray diffraction (WXRD) pattern of the Level-1 mesoporous TiO_2 superstructure (Figure 2a) reveals that all the

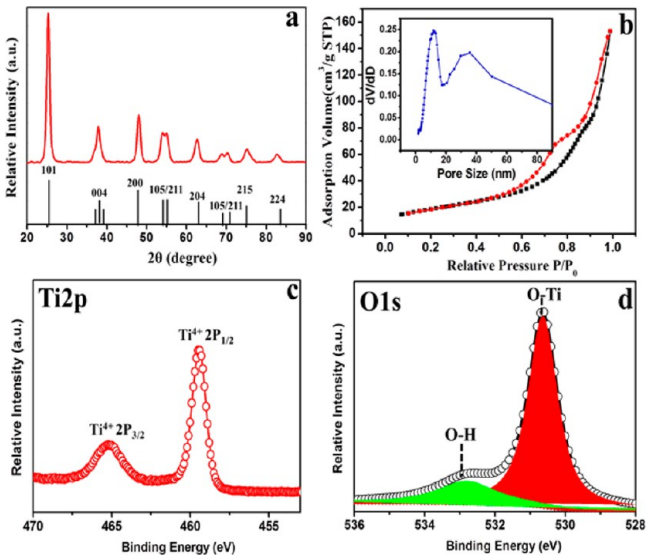

Figure 2. Characterization of the Level-1 mesoporous TiO_2 superstructures. (a) The WAXRD pattern of the Level-1 mesoporous TiO_2 superstructures, compared to the standard anatase (space group $I4_1/amd$, JCPDS card No. 21-1272). (b) Nitrogen adsorption−desorption isotherms, and (inset) pore size distribution of the Level-1 mesoporous TiO_2 superstructure. (c, d) XPS core-level spectra of O 1s and Ti 2p of the Level-1 mesoporous TiO_2 superstructure.

diffraction peaks match well with anatase phase (space group $I4_1/amd$).[46] Nitrogen adsorption−desorption isotherms show characteristic type IV curves with two distinguishable capillary condensation steps (Figure 2b). A distinct capillary condensation step at a relative pressure P/P_0 = 0.50−0.80 reflects uniform cylindrical mesopores resulted from the radial primary channels of the Level-1 mesoporous TiO_2 superstructure. A hysteresis loop at a higher pressure (P/P_0 = 0.90−0.99) may reflect the interchannel macropores between neighboring hemispherical posies. The pore size distribution calculated by Barrett−Joyner−Halenda (BJH) model (Inset of Figure 2b) is centered at about 6.5 nm, which agrees well with that (~6.0 nm) estimated from the SEM and TEM analyses. The BET surface area and pore volume are calculated to be as high as 134 m^2/g and 0.48 cm^3/g, respectively. The X-ray photoelectron

DOI: 10.1021/jacs.6b11641
J. Am. Chem. Soc. 2017, 139, 517−526

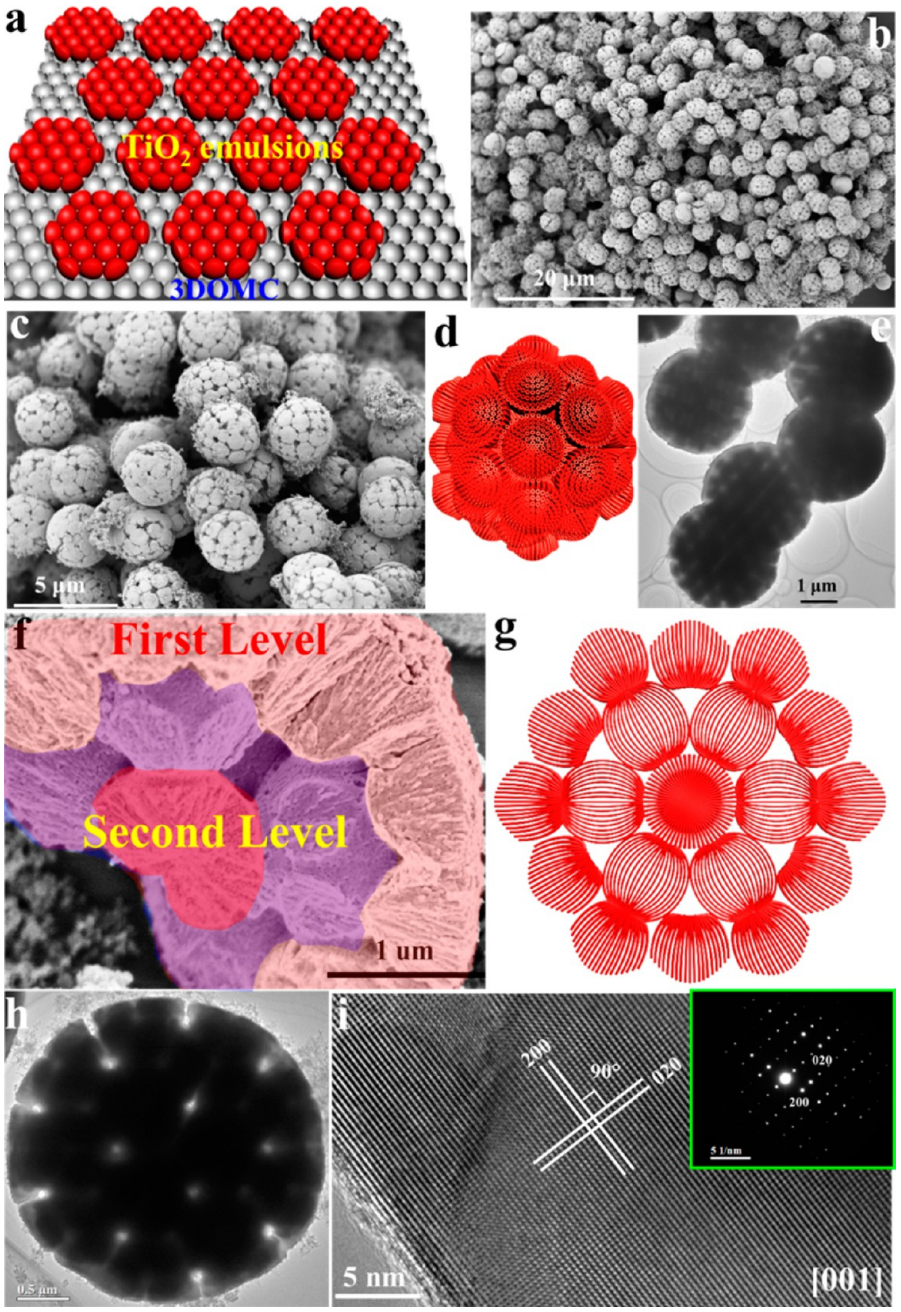

Figure 3. Mesoporous 3-D bouquet-posy-like TiO_2 superstructures (Level-2). (a) Schematic representation of the nucleation and growth of the Level-2 3-D bouquet-posy-like TiO_2 gel microemulsions (~3.5 μm in diameter) within 3-D ordered macroporous carbon (3DOMC) scaffolds. (b, c) SEM images of the Level-2 mesoporous TiO_2 superstructure after calcination in air at 400 °C for 2 h. (d) The structure model of a Level-2 mesoporous TiO_2 superstructure, showing its 3-D bouquet-posy-like topology (13 spherical cores and 44 satellite hemispheres) with radially oriented mesopore channels. (e) The TEM image of the Level-2 mesoporous TiO_2 superstructure. (f) The SEM image of a single ultramicrotomed Level-2 mesoporous TiO_2 superstructure. (g) The corresponding interior mesopore model. (h) The TEM image of a single Level-2 mesoporous TiO_2 superstructure. (i) HRTEM image taken from the area of the cylindrical mesopore bundles of an ultramicrotomed Level-2 mesoporous TiO_2 superstructure with [001] incidence. Inset of panel I is the corresponding SAED pattern.

spectroscopy (XPS) of Ti_{2p} ($Ti_{2p3/2}$, binding energy 464.2 eV; $Ti_{2p1/2}$ of 458.5 eV) is identical to Ti^{4+} oxidation state[47] (Figure 2c). The O 1s XPS spectrum shows two chemical states of oxygen (Figure 2d). The sharp peak at 530.6 eV is assigned to anatase lattice oxygen of O−Ti. Another satellite peak at 532.8 eV comes from O−H bonds, indicating massive Ti−OH groups on the (001) surface of the single-crystalline anatase walls.[42,47,48]

The architectural complexity and symmetry can precisely be controlled by tuning the size of impregnated TiO_2 precursor gel emulsion droplet. Typically, when the size of TiO_2 precursor gel emulsion is increased to be ~3.5 μm (Figure S7), a more complex Level-2 TiO_2 superstructure with an unprecedented 12-fold symmetry and configuration is formed within 3DOMC scaffolds (Figure 3a). SEM and TEM images show that the Level-2 mesoporous TiO_2 superstructures retain a uniform hierarchical spherical morphology (~3.0 μm in diameter) with

DOI: 10.1021/jacs.6b11641
J. Am. Chem. Soc. 2017, 139, 517−526

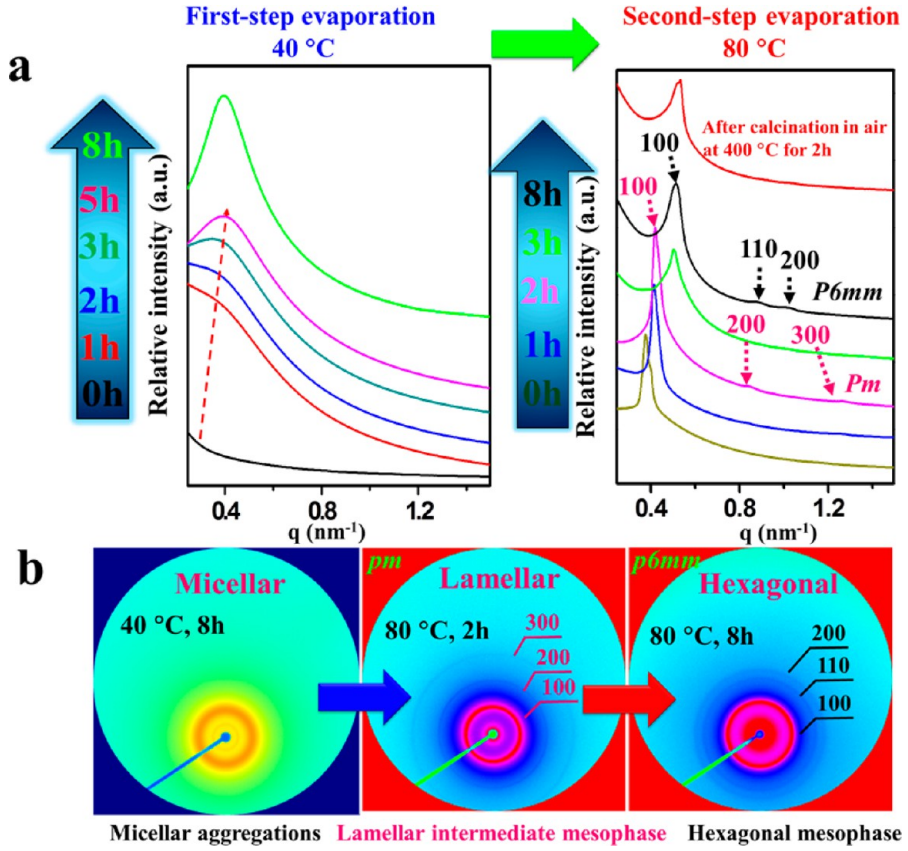

Figure 4. Representation of the formation process of 3-D mesoporous bouquet-posy-like TiO_2 superstructures. (a) *In-situ* time-resolved synchrotron radiation 1-D SAXS patterns of the Level-1 mesoporous TiO_2 superstructure products harvested at different intervals of reaction. (b) *In-situ* synchrotron radiation 2-D SAXS patterns of the Level-2 mesoporous TiO_2 superstructure products harvested at different intervals of reaction time.

a high degree of architectural complexity and symmetry after the removal of the 3DOMC scaffolds by calcination in air (Figure 3b–e and Figure S8). The single ultramicrotomed Level-2 mesoporous TiO_2 superstructure is composed of two well-defined levels of architectural arrangements (Figure 3f,g and Figure S9 and S10). The first level is composed a spherical mesoporous core with a diameter of ~800 nm and up to 12 satellite mesoporous spheres epitaxially growing out from the core vertices. The second level is composed of up to 44 branched mesoporous hemispheres (with a radius of ~400 nm), which are epitaxially grown out from the second satellite spheres.

As for the Level-1 mesoporous TiO_2 superstructure, all cylindrical open mesopore channels of Level-2 mesoporous TiO_2 superstructure are radially grown from the center to the surface within all spherical cores, 12 satellite spheres, and 44 branched hemispheres (Figure 3h). The cylindrical pores are well interconnected between 12 satellite spheres and 44 branched hemispheres, and even the center solid sphere, and they extended throughout the whole Level-2 TiO_2 superstructure (Figure S9). The Level-2 mesoporous TiO_2 superstructure has also well-defined single-crystalline anatase nature of each mesoporous hemispherical unit (Figure 3i and Figure S11). The BET surface area and pore volume of the Level-2 mesoporous TiO_2 superstructure are determined to be as high as 148 m^2/g and 0.51 cm^3/g (Figure S12), a little higher than that of the Level-1 mesoporous TiO_2 superstructure (134 m^2/g and 0.48 cm^3/g).

To investigate the growth process of the 3-D mesoporous bonquet-posy-like TiO_2 superstructures, we utilized *in situ* synchrotron radiation small-angle X-ray scattering (SAXS) technique to examine the products harvested at different intervals of the reaction. Initially, no ordered phase is detected after a TiO_2 liquid precursor solution infiltration within 3DOMC scaffolds (Figure 4a). After the first-step evaporation at 40 °C for 1 h, a broad peak centered at about q = 0.4 nm^{-1} is observed. The intensity of the micellar scattering peak increases rapidly with the extended evaporation time from 2 to 5 h (at 40 °C). After continuous first-step evaporation at 40 °C for 8 h, the main peak shifts to a lower q value (0.3 nm^{-1}) (Figure 4). This lower q value is the scattering originating from F123 micelles aggregated in flocs by the polymerizing titania oligomers. The intensity of the micellar scattering increases with time, which is attributed to an increased electron density contrast due to the adsorption of titania oligomers to the PEO groups of the amphiphile. *In-situ* TEM images further confirm that these spherical PEO–PPO–PEO/TiO_2 composite micelles with an average diameter of about 12.5 nm are well self-assembled within 3DOMC scaffolds (Figure S13). These uniform spherical micelles possess a typical core–shell structure with PEO–PPO–PEO as a core and titania oligomers as a shell (Figure S13b–d and Figure S14). It is worth noting that a shift to higher q value of reflections in the patterns is observed with the first-step solvent evaporation at 40 °C from 1 to 5 h, which corresponds to a decrease in the unit cell parameter owing to an increase in titania condensation. With a second-step evaporation at 80 °C for 2 h, three well-defined reflections at q = 0.42, 0.84, and 1.26 nm^{-1} clearly appear (Figure 4a), which can be indexed as the 100, 200, and 300 reflections of a 2-D lamellar mesophase. The confined TiO_2 gel microemulsions

DOI: 10.1021/jacs.6b11641
J. Am. Chem. Soc. 2017, 139, 517–526

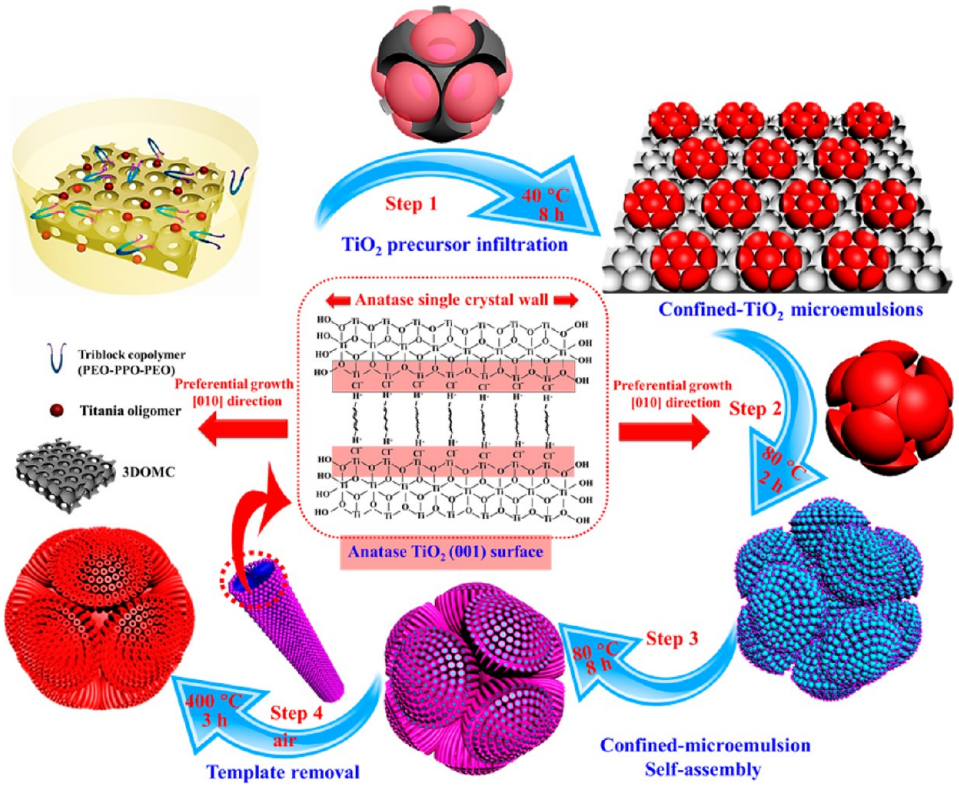

Figure 5. Schematic representation of the formation process through confined-micromulsion self-assembly process. Step 1: the formation of uniform TiO_2 micelles-based microemusion droplets due to the increasing surface tension with the initial preferential evaporation of THF solvent at 40 °C for 8 h. Step 2: A second-step evaporation at 80 °C actually drives the spherical micelles within TiO_2 microemusion droplet to self-assemble into an intermediate lamellar intermediate mesophase. Step 3: The continuous second-step evaporation at 80 °C not only drives the micelles to further fuse into radially oriented cylindrical micelles but also drives TiO_2 oriented growth around F127 cylindrical micelles to form a single-crystal anatase wall. Step 4: The Level-2 mesoporous TiO_2 superstructures are obtained by removing the triblock copolymer and 3DOMC templates and after calcination in air at 400 °C for 2 h.

within 3DOMC experience a short lamellar intermediate mesophase, and then turn into a 2-D hexagonal mesophase with the 100, 110, and 200 reflections at q = 0.51, 0.88, and 1.02 nm^{-1} after an evaporation at 80 °C for 6 h (Figure 4a,b). Summarizing the above *in situ* SAXS results, we can conclude that the two-step evaporations can lead to a mesostructural transformation of the TiO_2-oligomer/Pluronic composite microemulsions from initial spherical micellar aggregations to a lamellar, and finally to hexagonal mesophase within 3DOMC scaffolds. Without using 3DOMC scaffolds as a confined space, only uniform mesoporous TiO_2 solid microspheres (Level-0, ~800 nm in diameter) with radially oriented mesochannels are formed after the two-step evaporations (Figure S15).[42]

Based on the above observations, we propose that the growth of the 3-D bouquet-posy-like mesoporous TiO_2 superstructures proceeds through a confined-microemulsion self-assembly process (Figure 5). With the first-step preferential evaporation of THF solvent at a low temperature of 40 °C, the TiO_2 precursor solution becomes viscous, and tetrabutyl titanate (TBOT) is slowly hydrolyzed and assembled with amphiphilic Pluronic F127 to form uniform spherical PEO−PPO−PEO/TiO_2 composite micelles at the liquid−liquid phase interface. With the continuous THF evaporation at 40 °C (first-step evaporation), the composite micelles begin to nucleate and aggregate in the macropore cavities of 3DOMC scaffolds. In the meantime, the surface tension of the solution is dramatically increased over its concentration, thereby allowing the TiO_2 precursor aqueous to separate into uniform micelle-based microemulsion droplets that are more easily suspended within confined voids of 3DOMC scaffolds. It is worth to mention that the formation of the spherical core and 12 symmetric satellite hemispheres has undergone an interface tension-induced shrinkage procedure (Figure 5). With THF evaporation, the increasing interface tension force tends to pull the formed microemulsion droplets, completely filling of the center macropores of 3DOMCs, which can lead to forming a spherical core at the microemulsion droplets' center. Meanwhile, with the continuous evaporation of THF, the volume of the microemulsion droplets in macropores is dramatically decreased, and the shrinkage of microemulsion droplets occurs during THF evaporation, which makes one spherical core coupled with 12 satellite hemispheres via 12 connected macropore windows of the 3DOMC scaffolds. Under the same confined-microemulsion self-assembly procedure, a Level-2 TiO_2 gel microemulsion with 13 solid spheres and up to 44 branched hemispheres can be well colloidal lithographed within 3DOMC scaffolds by doubling the content of impregnated TiO_2 precursor. Subsequently, a second-step evaporation of residual THF and the hydrolyzed *n*-butyl alcohol in the solids at 80 °C actually drives the spherical micelles within the TiO_2 gel microemulsion droplets to self-assemble into an intermediate lamellar mesophase, and such second-step evaporation can further drive the lamellar intermediate mesophase to fuse into a radially oriented 2D hexagonal phase. Owing to the strong second-step evaporation-induced driving force, the cylindrical mesopore channels are well interconnected and

DOI: 10.1021/jacs.6b11641
J. Am. Chem. Soc. 2017, 139, 517−526

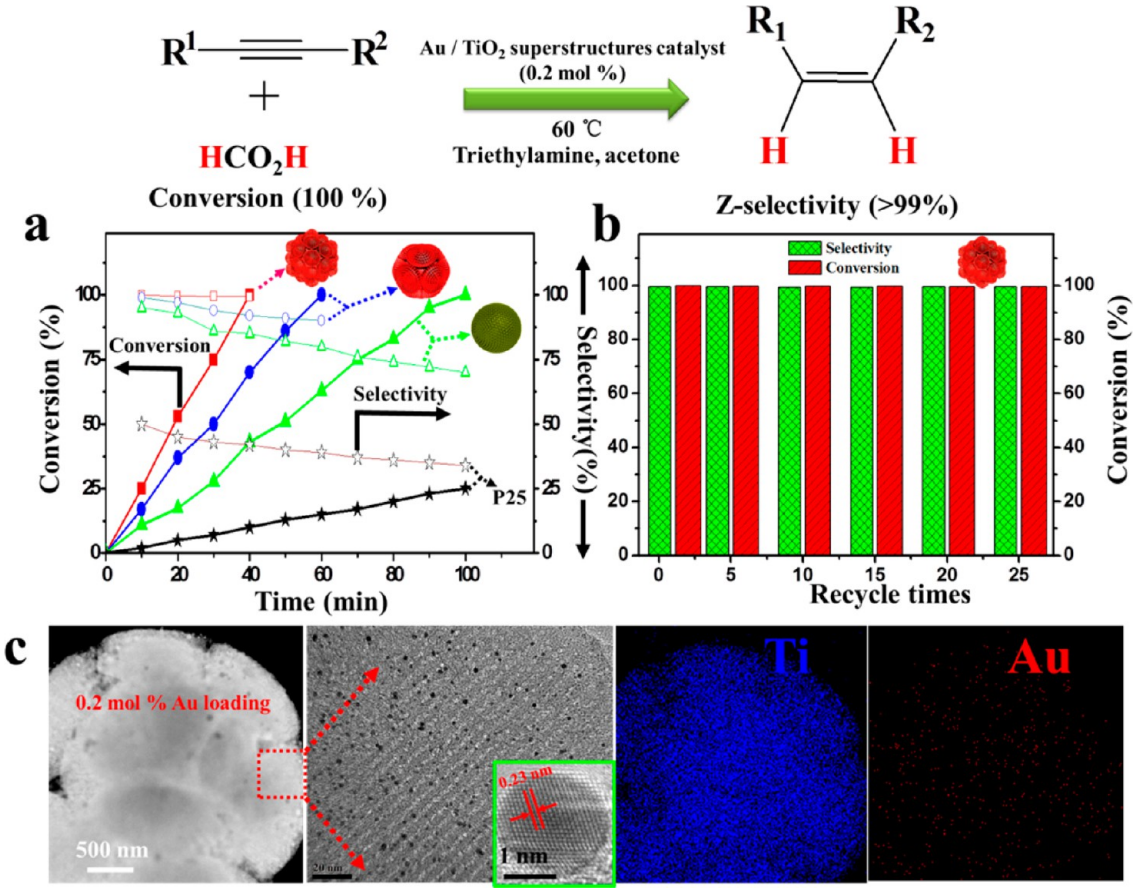

Figure 6. Semihydrogenation performance of the 3-D mesoporous bouquet-posy-like TiO_2 superstructure supported catalysts. (a) Diphenylacetylene conversion and selectivity in *cis*-stilbene with the reaction time for the first run. Squares, the Au/Level-2 mesoporous TiO_2 superstructure catalysts (loading 0.2 mol % Au). (●) Au/Level-1 mesoporous TiO_2 superstructure catalysts (0.2 mol % Au). (▲) Au/Level-0 mesoporous TiO_2 microsphere catalysts (0.2 mol % Au). (★) Au/commercial TiO_2 (P25) catalysts (0.2 mol % Au). Solid symbols indicate conversion, and hollow symbols indicate selectivity. (b) Recycle performance of diphenylacetylene conversion and selectivity in *cis*-stilbene on Au/Level-2 mesoporous TiO_2 superstructure catalyst (0.2 mol % Au). (C) HAADF-STEM image, TEM, and EDX elemental maps of Ti, O, Au recorded on an ultramicrotomed Au/Level-2 mesoporous TiO_2 superstructure catalyst (0.2 mol % Au), showing that the Au nanoparticles (~3 nm) are uniformly immobilized within mesochannels of Level-2 mesoporous TiO_2 superstructures. The semihydrogenation reaction conditions: diphenylacetylene (0.5 mmol), formic acid (2.5 mmol), trimethylamine (1.6 mmol), acetone (2 mL), catalyst (20 mg), 60 °C.

radially distributed within the whole TiO_2 superstructures. Finally, after removing triblock copolymer F127 template and 3DOMC scaffolds by calcination in air, 3-D mesoporous TiO_2 superstructures with different levels of bouquet-posy topologies with radially oriented and well-interconnected mesochannels are obtained.

The oriented growth of the single-crystal anatase pore walls with dominant (001) active facets here is related to the solvent evaporation driven-oriented assembly growth process.[41,42] As shown in Figure 5, the addition of a strong aqueous acid (HCl) can not only retard hydrolysis of titanium precursor but also charge the initially formed anatase nanocrystals with high surface energy by selective adsorption of Cl^- ions on (001) plane,[44] which may act as a strong "bridge" between the nanocrystal building blocks and hydrophilic segment boundary of Pluronic F127. As confirmed by *in situ* synchrotron radiation SAXS patterns (Figure 4a), the continuous second-step evaporation at 80 °C can actually drive the initially formed spherical micelles to fuse into radially oriented cylindrical micelles. Simultaneously, such second-step evaporation from center to outside can also incidentally drive TiO_2 crystallization oriented around F127 cylindrical micelles due to their strong coupling action. Our previous work[42] has also confirmed that such slow evaporation and confinement of the triblock copolymer hydrophilic boundary could correct the crystallographic orientation of the TiO_2 nanocrystal building blocks. After calcination at 400 °C for 2 h, these oriented anatase nanocrystals can further crystallize into single-crystal walls with (001) as the dominantly exposed facets within TiO_2 superstructures.

cis-Semihydrogenation of alkynes is here chosen as a model reaction to evaluate the catalytic activity of the 3-D mesoporous bouquet-posy-like TiO_2 superstructure supported catalysts. The semihydrogenation is one of the most simple and straightforward methods to prepare alkenes in the laboratory as well as in industry; however, it often suffers over-reduction due to the difficulty of the control of a stoichiometric amount of H_2. By using biorenewable formic acid (HCOOH) as the hydrogen source,[49,50] Au/Level-2 mesoporous TiO_2 superstructure catalyst (0.2 mol % Au) displays 100% diphenylacetylene conversion within 40 min, and the selectivity to cis-stilbene is measured to be ≥99% (Figure 6a). In contrast, the Au/Level-1 mesoporous TiO_2 superstructure catalyst displays 70% diphenylacetylene conversion and 92% *cis*-stilbene selectivity within 40 min. The diphenylacetylene conversion and *cis*-stilbene selectivity of the Au/Level-0 mesoporous TiO_2

DOI: 10.1021/jacs.6b11641
J. Am. Chem. Soc. 2017, 139, 517−526

microspheres (0.2 mol % Au, Figure S16) decrease to 43% and 85%, respectively. Only 10% diphenylacetylene conversion and 42% *cis*-stilbene selectivity can be achieved for Au/commercial TiO_2 (P25) catalyst (0.2 mol % Au). The above results clearly illustrate the fact that with the higher degree of mesoporous architectural complexity and symmetry, higher activity and selectivity can be achieved for Au/TiO_2-based catalysts. The reaction rate of the Au/Level-2 mesoporous TiO_2 superstructure catalyst (214 mol/(h·g)) is 10 times higher than that of the Au/commercial TiO_2 (P25) catalyst (20 mol/(h·g)). The substrate applicability of the Au/Level-2 mesoporous TiO_2 superstructure catalyst is further investigated using various alkynes in a batch reactor. As illustrated in Table S1, a wide range of aromatic and aliphatic terminal alkynes are converted to the corresponding alkenes with a high conversion (≥99.7%) and selectivity (≥96%). The Au/Level-2 mesoporous TiO_2 superstructure catalyst can be easily recovered by filtration and retains its high activity and selectivity during 25 recycling experiments (Figure 6b), demonstrating its high durability.

The high activity, selectivity, and recyclability of the Au catalysts supported on the 3-D mesoporous bouquet-posy-like TiO_2 can be well attributed to their unique superstructures with high architectural complexity, high accessible surface area, radially oriented and highly interconnected mesochannels, and single-crystalline walls with dominant (001) active facets. In this semihydrogenation reaction, one posy hemisphere here is assumed as a single nanoreactor unit, which can provide 3-D radially oriented open mesochannels and single-crystalline walls for immobilizing Au nanoparticles (with uniform size of ~3 nm, Figure 6c and Figure S16) for semihydrogenation reaction. With this in mind, a Level-2 mesoporous TiO_2 superstructure can contribute up to 70 hemispherical nanoreactor units, which is about 5 times higher than the Level-1 TiO_2 superstructure (14 hemispherical nanoreactor units) and even 36 times higher than the Level-0 microspheres (2 hemispherical nanoreactor units). The higher the levels, the more reaction spaces are provided and thus the higher activity and selectivity can be achieved for semihydrogenation reaction. Moreover, the radially oriented open mesochannels can provide individual quasi-confined nanospaces to prevent aggregation of Au nanoparticles, which may explain the excellent reusability of the bouquet-posy-like mesoporous TiO_2 superstructures.

3. CONCLUSIONS

In summary, well-defined, uniform 3-D open highly ordered mesoporous TiO_2 superstructures with bouquet-posy-like topologies, radially oriented mesochannels, and single-crystalline pore walls have successfully been synthesized by a novel confined-micromulsion self-assembly method. Such unprecedented mesoporous TiO_2 superstructure (Level-1) consists of 1 spherical core and 12 symmetric branched hemispheres epitaxially growing out of the core vertices. A more complex and asymmetric TiO_2 superstructure (Level-2) with 13 spherical cores and up to 44 symmetric satellite hemispheres can also be well manipulated by increasing the size or content of impregnated TiO_2 precursor emulsion droplets. The bouquet-posy-like mesoporous TiO_2 superstructures possess high accessible surface area (134−148 m^2/g), large pore volume (0.48−0.51 cm^3/g), and well single-crystalline anatase walls with dominant (001) active facets. All cylindrical mesochannels are highly interconnected from center to outside and radially distributed within the whole TiO_2 superstructure, and all TiO_2 nanocrystal building blocks are oriented into a single-crystal anatase wall, making them highly active in *cis*-semihydrogenation reaction. The mesoporous TiO_2 superstructure supported catalysts showed the excellent catalytic conversion (≥99.7%) and *Z*-selectivity (≥96%) in *cis*-semihydrogenation of various alkynes at a low temperature of 60 °C. This confined-micromulsion self-assembly method is expected to synthesize other semiconductor superstructures with unprecedented topologies, oriented mesopore channels, and single-crystal nature for advanced applications in catalysis, sensors, drug delivery, optoelectronic, etc.

4. EXPERIMENTAL SECTION

4.1. Preparation of Resol Precursor. For a typical preparation, 8.0 g of phenol was melted at 42 °C, and then 2.0 g of 20 wt % NaOH aqueous solution was added slowly under stirring. After 10 min, 14.5 g of formalin solution (37 wt % formaldehyde) was added dropwise, and the reaction mixture was stirred at 70 °C for 1 h. Upon cooling of the mixture to room temperature, the pH value was adjusted to be about 6.0 by adding HCl solution (2.0 M). Water was then removed out under vacuum below 50 °C. The resol precursors were redissolved in ethanol (20 wt % ethanolic solution), and the sodium chloride was separated as a precipitate at the same time.

4.2. Preparation of Polystyrene Colloidals and Macroporous Carbon Inverse Scaffolds. Monodisperse polystyrene (PS) microspheres with a mean size of 1.0 μm were prepared through a dispersion polymerization approach. For a typical preparation, 8.0 g of styrene, 0.06 g of polyvinylpyrrolidone (PVP, M_w = 30000), 12 mL of H_2O, and 0.15 g of ammonium peroxodisulfate (APS) were dissolved in 100 mL of ethanol. The obtained solution was then added into a 250-mL three-neck round-bottom flask with a magnetic stirrer, a refluxing condenser, and a nitrogen inlet. After sealing in a nitrogen atmosphere, the reactor was submerged in an oil bath, and the polymerization was carried out at 70 °C for 15 h. Then, the obtained PS microspheres were washed with water and redispersed in 50 mL of ethanol. The PS dispersed solution was obtained and placed in an oven at 40 °C for 3 days until the ethanol was completely evaporated. Finally, the monolithic PS colloidal crystals were obtained.

For the preparation of macroporous carbon scaffolds, 5.0 mL of the resol precursor obtained above was cast dropwise on the colloidal crystals (5.0 g). After the evaporation of ethanol for 12 h at 40 °C, the dried monolith was heated in an oven at 80 °C for 3 h. Finally, three-dimensional (3-D) ordered macroporous carbon inverse scaffolds (3DOMCs) with a diameter of about 800 nm were obtained after the calcination of PS/phenolic resin composite at 450 °C for 3 h under N_2.

4.3. Preparation of TiO_2 Precursor Solution. The TiO_2 precursor solution was prepared by mixing with 1.5 g of Pluronic F127, 2.4 g of concentrated HCl, 2.4 g of CH_3COOH, 3.4 g of tetrabutyl titanate (TBOT), 0.2 g of H_2O, and 30 mL of tetrahydrofuran (THF). The mixed solution was vigorously stirred for 30 min to form a clear and transparent yellow solution.

4.4. Synthesis of Level-0 Mesoporous TiO_2 Microspheres (~800 nm in Diameter). The Level-0 mesoporous TiO_2 microspheres were synthesized by an evaporation-driven oriented assembly (EDOA) approach.[1] Typically, 30 mL of the TiO_2 precursor solution was transferred into a volumetric flask and left in a drying oven to evaporate THF at 40 °C for 20 h; then second-step was evaporation at 80 °C for another 8 h to completely remove the solvents. After that, the obtained milky white precipitate was heated in N_2 at 350 °C for 2 h and then in air at 400 °C for 3 h to remove F127 copolymer templates, and Level-0 mesoporous TiO_2 microspheres (~800 nm in diameter) were finally obtained.

4.5. Synthesis of Level-1 Mesoporous TiO_2 Superstructure (~1.6 μm in Diameter). A piece of 3DOMC plates (3 cm × 3 cm × 1.5 cm, 2.5 g in total) was soaked in 8 mL of the TiO_2 precursor solution above for first-step evaporation at 40 °C for 20 h, and then second-step evaporation was carried out at 80 °C for another 8 h to completely remove the residual THF and the hydrolyzed *n*-butyl alcohol solvents. After that, the impregnated 3DOMC plate was heated in N_2 at 350 °C for 2 h and then in air at 400 °C for 3 h to

DOI: 10.1021/jacs.6b11641
J. Am. Chem. Soc. 2017, 139, 517−526

remove F127 copolymers and macroporous carbon scaffolds, respectively, and the Level-1 mesoporous TiO_2 superstructure (~1.6 μm in diameter) was finally obtained.

4.6. Synthesis of Level-2 Mesoporous TiO_2 Superstructure (~3.0 μm in diameter). A piece of 3DOMC plate (3 cm × 3 cm × 1.5 cm, 2.5 g in total) was soaked in 16 mL of the TiO_2 precursor solution for first-step evaporation at 40 °C for 20 h, and then second-step evaporation was carried out at 80 °C for another 8 h to completely remove the residual THF and hydrolyzed *n*-butyl alcohol solvents. After that, the impregnated 3DOMC plate was heated in N_2 at 350 °C for 2 h and then in air at 400 °C for 3 h to remove F127 copolymers and macroporous carbon scaffolds, respectively, and Level-2 mesoporous TiO_2 superstructure (~3.0 μm in diameter) was finally obtained.

4.7. Preparation of Au/Mesoporous TiO_2 Superstructure Catalyst (0.2 mol % Au). Immobilization of Au nanoparticles (with a size of ~2 nm) into the mesopore channels of the mesoporous TiO_2 superstructures was achieved via *in situ* growth approach to obtain Au catalysts supported on the mesoporous TiO_2 superstructures. In a typical process, 50 mg of the mesoporous TiO_2 superstructure was dispersed in 10 mL of deionized water via sonication. After the mixture was stirred for 15 min at 30 °C, 0.25 mL of fresh $HAuCl_4 \cdot 4H_2O$ aqueous solution at a concentration of 1.0 mg/mL was added dropwise and kept at 30 °C with stirring for 4 h. Then, 1.0 mL of 0.1 M $NaBH_4$ solution was added dropwise, and the mixture was aged at the same temperature for 24 h. The Au-loaded products were separated by centrifugation, washed with water and ethanol, and dried at 60 °C. For Au-loaded commercial P25 TiO_2 catalysts, the sample was prepared by the same method.

4.8. Catalytic Procedure for the Transfer Semireduction of Alkynes with Formic Acid. The mixture of alkyne (0.5 mmol), the Au-catalyst (Au, 0.2 mol %, 20 mg), formic acid (2.5 mmol), trimethylamine (1.6 mmol), and acetone (2.0 mL) was added to a flask (10 mL) equipped with a reflux condenser. The resulting mixture was allowed to reflux with vigorous stirring (800 rpm) at 60 °C for given reaction time. After completion of the reaction, the mixture was filtered, washed with water, and extracted with ethyl acetate. The reaction solution was concentrated and dried under reduced pressure to give the crude product, which was further purified by silica gel chromatography eluting with petroleum ether (60–90 °C)/ethyl acetate mixture. The products were analyzed by GC-MS. The conversion and selectivity were determined by GC-FID using *p*-xylene (PX) as an internal standard.

4.9. Materials Characterization. Synchrotron radiation small-angle X-ray scattering (SAXS) measurements were performed at Beamline BL16B of Shanghai Synchrotron Radiation Facility (SSRF). The *d*-spacing values were calculated from the formula $d = 2\pi/q$. Transmission electron microscopy (TEM), high-angle annular dark field imaging in the scanning TEM (HAADF-STEM), and energy dispersive spectroscopy (EDS) observations were performed on JEM-2100F transmission electron microscope with an accelerating voltage of 200 kV equipped with a postcolumn Gatan imaging filter (GIF-Tridium). To investigate the interior structures of the resulting mesoporous TiO_2 microspheres, the samples were embedded in a white resin and cut in ultramicrotome to thin sections with a thickness below 100 nm. Field-emission scanning electron microscopy (FESEM) images were collected on Hitachi model S-4800 field-emission scanning electron microscope. To obtain information on TiO_2 gel microemulsion droplets (Level-1 and Level-2) within 3DOMC scaffolds, cryo-scanning electron microscopy (cryo-SEM) images were taken after the TiO_2 gel microemulsion droplets were frozen by soil nitrogen. X-ray diffraction (XRD) patterns were recorded with a Bruker D8 powder X-ray diffractometer (Germany) using Cu Kα radiation (40 kV, 40 mA). Nitrogen sorption isotherms were measured at 77 K with a Micromeritics Tristar 3020 analyzer (USA). Before measurements, the samples were degassed in a vacuum at 180 °C for at least 6 h. The Brunauer–Emmett–Teller (BET) method was utilized to calculate the specific surface areas. By using the Barrett–Joyner–Halenda (BJH) model, the pore volumes and pore size distributions were derived from the adsorption branches of isotherms. X-ray photoelectron spectroscopy (XPS) was recorded on an AXIS ULTRA DLD XPS System with MONO Al source (Shimadzu Corp). Photoelectron spectra were recorded by using monochromatic Al K_R radiation under vacuum at 5×10^{-9} Pa. All of the binding energies were referenced to the C 1s peak at 284.6 eV of the surface adventitious carbon.

■ ASSOCIATED CONTENT

Supporting Information

The Supporting Information is available free of charge on the ACS Publications website at DOI: 10.1021/jacs.6b11641.

Supporting results of SEM images, TEM images, HAADF-STEM, SAED patterns, and BET measurement with literature (PDF)

■ AUTHOR INFORMATION

Corresponding Author

*dyzhao@fudan.edu.cn

ORCID

Yong Cao: 0000-0002-8333-0181

Dongyuan Zhao: 0000-0001-8440-6902

Author Contributions

#Yong Liu and Kun Lan contributed equally.

Notes

The authors declare no competing financial interest.

■ ACKNOWLEDGMENTS

This work is supported by the State Key Basic Research Program of China (2013CB934104), National Science Foundation NSFC (21210004), and Science & Technology Commission of Shanghai Municipality (08DZ2270500), Shanghai Leading Academic Discipline Project (B108), and Deanship of Scientific Research, Deanship of Scientific Research, The authors extend their appreciation to the International Scientific Partnership Program ISPP at King Saud University for funding this research work through ISPP# 0018, King Abdulaziz City for Science and Technology, Kingdom of Saudi Arabia, Award Research Project Number ADV1718-02, and Qatar University start-up grant no. QUSG-CAS-MST-14\15-1. Y.L. also acknowledges the China Postdoctoral Science Foundation (2015M580295) and International Postdoctoral Exchange Fellowship Program (No. 20160051).

■ REFERENCES

(1) Xia, Y.; Yin, Y.; Lu, Y.; McLellan, J. *Adv. Funct. Mater.* **2003**, *13*, 907.

(2) Wang, T.; Zhuang, J.; Lynch, J.; Chen, O.; Wang, Z.; Wang, X.; LaMontagne, D.; Wu, H.; Wang, Z.; Cao, Y. C. *Science* **2012**, *338*, 358.

(3) Ma, C. Y.; Mu, Z.; Li, J. J.; Jin, G. Y.; Cheng, J.; Lu, G. Q.; Hao, Z. P.; Qiao, S. Z. *J. Am. Chem. Soc.* **2010**, *132*, 2608.

(4) Xu, S.; Yan, Z.; Jang, K.-I.; Huang, W.; Fu, H.; Kim, J.; Wei, Z.; Flavin, M.; McCracken, J.; Wang, R.; et al. *Science* **2015**, *347*, 154.

(5) Suteewong, T.; Sai, H.; Hovden, R.; Muller, D.; Bradbury, M. S.; Gruner, S. M.; Wiesner, U. *Science* **2013**, *340*, 337.

(6) Gröschel, A. H.; Walther, A.; Löbling, T. I.; Schacher, F. H.; Schmalz, H.; Müller, A. H. *Nature* **2013**, *503*, 247.

(7) Hudson, Z. M.; Boott, C. E.; Robinson, M. E.; Rupar, P. A.; Winnik, M. A.; Manners, I. *Nat. Chem.* **2014**, *6*, 893.

(8) Wu, X.-J.; Chen, J.; Tan, C.; Zhu, Y.; Han, Y.; Zhang, H. *Nat. Chem.* **2016**, *8*, 470.

(9) Glotzer, S. C.; Solomon, M. J. *Nat. Mater.* **2007**, *6*, 557.

DOI: 10.1021/jacs.6b11641
J. Am. Chem. Soc. 2017, 139, 517–526

(10) Jiang, Y. W.; Carvalho-de-Souza, J. L.; Wong, R. C. S.; Luo, Z. Q.; Isheim, D.; Zuo, X. B.; Nicholls, A. W.; Jung, I. W.; Yue, J. P.; Liu, D.-J.; Wang, Y. C.; De Andrade, V.; Xiao, X. H.; Navrazhnykh, L.; Weiss, D. E.; Wu, X. Y.; Seidman, D. N.; Bezanilla, F.; Tian, B. Z. *Nat. Mater.* **2016**, *15*, 1023.
(11) Schreiber, R.; Do, J.; Roller, E.-M.; Zhang, T.; Schüller, V. J.; Nickels, P. C.; Feldmann, J.; Liedl, T. *Nat. Nanotechnol.* **2014**, *9*, 74.
(12) Zhang, H.; Yu, X.; Braun, P. V. *Nat. Nanotechnol.* **2011**, *6*, 277.
(13) Yin, Y.; Lu, Y.; Gates, B.; Xia, Y. *J. Am. Chem. Soc.* **2001**, *123*, 8718.
(14) Huang, X.; Yu, Y.; Jones, T.; Fan, H.; Wang, L.; Xia, J.; Wang, Z. J.; Shao, L. D.; Meng, X. M.; Willinger, M. G. *Adv. Mater.* **2016**, *28*, 7603.
(15) Guan, B. Y.; Yu, L.; Li, J.; Lou, X. W. *Sci. Adv.* **2016**, *2*, e1501554.
(16) Yang, T.; Zhou, R.; Wang, D.-W.; Jiang, S. P.; Yamauchi, Y.; Qiao, S. Z.; Monteiro, M. J.; Liu, J. *Chem. Commun.* **2015**, *51*, 2518.
(17) Hu, Y.; Gao, X.; Yu, L.; Wang, Y.; Ning, J.; Xu, S.; Lou, X. W. *Angew. Chem.* **2013**, *125*, 5746.
(18) Kim, K.; Lee, T.; Kwon, Y.; Seo, Y.; Song, J.; Park, J. K.; Lee, H.; Park, J. Y.; Ihee, H.; Cho, S. J.; Ryoo, R. *Nature* **2016**, *535*, 131.
(19) Ma, T. Y.; Dai, S.; Jaroniec, M.; Qiao, S. Z. *J. Am. Chem. Soc.* **2014**, *136*, 13925.
(20) Choi, M.; Na, K.; Kim, J.; Sakamoto, Y.; Terasaki, O.; Ryoo, R. *Nature* **2009**, *461*, 246.
(21) Schaedler, T. A.; Jacobsen, A. J.; Torrents, A.; Sorensen, A. E.; Lian, J.; Greer, J. R.; Valdevit, L.; Carter, W. B. *Science* **2011**, *334*, 962.
(22) Kraft, D. J.; Ni, R.; Smallenburg, F.; Hermes, M.; Yoon, K.; Weitz, D. A.; vanBlaaderen, A.; Groenewold, J.; Dijkstra, M.; Kegel, W. K. *Proc. Natl. Acad. Sci. U. S. A.* **2012**, *109*, 10787.
(23) Liu, Y.; Deng, Y. H.; Sun, Z. K.; Wei, J.; Zheng, G. F.; Asiri, A. M.; Khan, S. B.; Rahman, M. M.; Zhao, D. Y. *Small* **2013**, *9*, 2702.
(24) Guan, B. Y.; Yu, L.; Lou, X. W. *J. Am. Chem. Soc.* **2016**, *138*, 11306.
(25) Guan, B. Y.; Yu, L.; Lou, X. W. *Adv. Mater.* **2016**, *28*, 9596.
(26) Wei, B.; Dai, M.; Yin, P. *Nature* **2012**, *485*, 623.
(27) Castro, C. E.; Kilchherr, F.; Kim, D.-N.; Shiao, E. L.; Wauer, T.; Wortmann, P.; Bathe, M.; Dietz, H. *Nat. Methods* **2011**, *8*, 221.
(28) Ke, Y.; Ong, L. L.; Shih, W. M.; Yin, P. *Science* **2012**, *338*, 1177.
(29) Gao, W.; Feng, X.; Pei, A.; Kane, C. R.; Tam, R.; Hennessy, C.; Wang, J. *Nano Lett.* **2014**, *14*, 305.
(30) Luo, Z.; Jiang, Y.; Myers, B. D.; Isheim, D.; Wu, J.; Zimmerman, J. F.; Wang, Z.; Li, Q.; Wang, Y.; Chen, X.; et al. *Science* **2015**, *348*, 1451.
(31) Urban, A. S.; Shen, X.; Wang, Y.; Large, N.; Wang, H.; Knight, M. W.; Nordlander, P.; Chen, H.; Halas, N. J. *Nano Lett.* **2013**, *13*, 4399.
(32) Deng, Y. H.; Qi, D.; Deng, C.; Zhang, X.; Zhao, D. Y. *J. Am. Chem. Soc.* **2008**, *130*, 28.
(33) Richman, E. K.; Brezesinski, T.; Tolbert, S. H. *Nat. Mater.* **2008**, *7*, 712.
(34) Oveisi, H.; Jiang, X.; Imura, M.; Nemoto, Y.; Sakamoto, Y.; Yamauchi, Y. A. *Angew. Chem., Int. Ed.* **2011**, *50*, 7410.
(35) Weng, W.; Higuchi, T.; Suzuki, M.; Fukuoka, T.; Shimomura, T.; Ono, M.; Radhakrishnan, L.; Wang, H.; Suzuki, N.; Oveisi, H.; Yamauchi, Y. *Angew. Chem., Int. Ed.* **2010**, *49*, 3956.
(36) Du, X.; Qiao, S. Z. *Small* **2015**, *11*, 392.
(37) Wen, C. Z.; Jiang, H. B.; Qiao, S. Z.; Yang, H. G.; Lu, G. Q. J. *J. Mater. Chem.* **2011**, *21*, 7052.
(38) Shan, F.; Lu, X.; Zhang, Q.; Wu, J.; Wang, Y.; Bian, F.; Lu, Q.; Fei, Z.; Dyson, P. J. *J. Am. Chem. Soc.* **2012**, *134*, 20238.
(39) Walcarius, A.; Sibottier, E.; Etienne, M.; Ghanbaja, J. *Nat. Mater.* **2007**, *6*, 602.
(40) Yamauchi, Y.; Sawada, M.; Noma, T.; Ito, H.; Furumi, S.; Sakka, Y.; Kuroda, K. *J. Mater. Chem.* **2005**, *15*, 1137.
(41) Liu, Y.; Che, R.; Chen, G.; Fan, J.; Sun, Z.; Wu, Z.; Wang, M.; Li, B.; Wei, J.; Wei, Y.; Wang, G.; Guan, G. Z.; Elzatahry, A. A.; Bagabas, A. A.; Al-Enizi, A. M.; Deng, Y. H.; Peng, H. S.; Zhao, D. Y. *Sci. Adv.* **2015**, *1*, e1500166.
(42) Liu, Y.; Luo, Y.; Elzatahry, A. A.; Luo, W.; Che, R.; Fan, J. W.; Lan, K.; Al-Enizi, A. M.; Sun, Z. K.; Li, B.; Liu, Z. W.; Shen, D. K.; Ling, Y.; Wang, C.; Wang, J. X.; Gao, W. J.; Yao, C.; Yuan, K. P.; Peng, H. S.; Tang, Y.; Deng, Y. H.; Zheng, G. F.; Zhou, G.; Zhao, D. Y. *ACS Cent. Sci.* **2015**, *1*, 400.
(43) Liu, Y.; Lan, K.; Bagabas, A. A.; Zhang, P. F.; Gao, W. J.; Wang, J.; Sun, Z. K.; Fan, J. W.; Elzatahry, A. A.; Zhao, D. Y. *Small* **2016**, *12*, 860.
(44) Yang, H. G.; Sun, C. H.; Qiao, S. Z.; Zou, J.; Liu, G.; Smith, S. C.; Cheng, H. M.; Lu, G. Q. *Nature* **2008**, *453*, 638.
(45) Crossland, E. J.; Noel, N.; Sivaram, V.; Leijtens, T. J.; Alexander-Webber, A.; Snaith, H. J. *Nature* **2013**, *495*, 215.
(46) Liu, Y.; Elzatahry, A. A.; Luo, W.; Lan, K.; Zhang, P.; Fan, J.; Wei, Y.; Wang, C.; Deng, Y. H.; Zheng, G. F.; Zhang, F.; Tang, Y.; Mai, L. Q.; Zhao, D. Y. *Nano Energy* **2016**, *25*, 80.
(47) Liu, Y.; Chen, L.; Hu, J.; Li, J. L.; Richards, R. *J. Phys. Chem. C* **2010**, *114*, 1641.
(48) Yang, H. G.; Liu, G.; Qiao, S. Z.; Sun, C. H.; Jin, Y. G.; Smith, S. C.; Zou, J.; Cheng, H. M.; Lu, G. Q. *J. Am. Chem. Soc.* **2009**, *131*, 4078.
(49) Li, S. S.; Tao, L.; Wang, F. Z. R.; Liu, Y. M.; Cao, Y. *Adv. Synth. Catal.* **2016**, *358*, 1410.
(50) Wagh, Y. S.; Asao, N. *J. Org. Chem.* **2015**, *80*, 847.

DOI: 10.1021/jacs.6b11641
J. Am. Chem. Soc. 2017, 139, 517−526